

Cite this: *J. Mater. Chem. A*, 2019, 7, 15633Received 16th April 2019  
Accepted 6th June 2019

DOI: 10.1039/c9ta04025k

rsc.li/materials-a

## A 3D ordered hierarchically porous non-carbon electrode for highly effective and efficient capacitive deionization†

Yuchen Wu,<sup>‡ab</sup> Gaopeng Jiang,<sup>ID ‡a</sup> Guihua Liu,<sup>a</sup> Gregory Lui,<sup>a</sup> Zachary Paul Cano,<sup>a</sup> Qian Li,<sup>a</sup> Zhen Zhang,<sup>ID a</sup> Aiping Yu,<sup>ID \*a</sup> Zisheng Zhang<sup>\*b</sup> and Zhongwei Chen<sup>ID \*a</sup>

In this work, three-dimensional ordered mesoporous titanium nitride (3DOM-TiN) has been synthesized *via* a templating method as a novel high-performance non-carbon capacitive deionization (CDI) electrode material. The dual ion electrosorption mechanisms, fast ion diffusion and rapid charge transfer enabled by the multiple advantageous features of the 3DOM-TiN electrode facilitate an outstanding CDI salt adsorption capacity (SAC) as high as 23.6 mg g<sup>-1</sup> and a record-breaking maximum salt adsorption rate (SAR) of 3.2 mg g<sup>-1</sup> min<sup>-1</sup> in 500 mg L<sup>-1</sup> NaCl solution at an applied voltage of 1.2 V. Such excellent CDI performance in addition to excellent cycling stability not only ranks the 3DOM-TiN electrode as one of the most promising electrodes for future CDI applications but also confirms the great potential of nanoengineered non-carbon electrodes for next-generation CDI cells.

The freshwater crisis has become one of the most challenging and urgent global issues due to the growing human population and pollution levels.<sup>1</sup> The ideal solution to this issue is the development of sustainable desalination technology, which can treat abundant saline and brackish water.<sup>2-4</sup> Current technologies include distillation, reverse osmosis, and electrodialysis. However, these technologies suffer from major drawbacks such as high capital cost and secondary pollution.<sup>4</sup> Alternatively, a highly efficient, low-cost, scalable and environmentally benign desalination technology known as capacitive deionization (CDI) has emerged as a viable and promising solution over the last two decades.<sup>5-8</sup> CDI applies the principle of ion electrosorption to remove charged ions in low salinity solutions such as brackish water.<sup>9</sup> Due to their similarity to

a supercapacitor,<sup>10,11</sup> CDI electrode materials play a pivotal role in the CDI performance. The majority of reported CDI electrodes are carbonaceous materials, from the earliest activated carbon (AC) electrode to the most recent carbon nanomaterial electrodes.<sup>12-18</sup> However, these carbonaceous CDI electrodes still suffer from low CDI performance, especially low salt adsorption capacity (SAC) and low salt adsorption rate (SAR).<sup>9</sup> Due to the strong dependence on electrostatic double-layer capacitance (EDLC) to remove ions from the solution, the improvement of SAC for carbonaceous CDI electrodes will be limited. The lack of tuning of the pore structure for these hydrophobic carbonaceous electrodes causes inaccessible surfaces and unfavorable tortuous microporous channels for ions to diffuse, leading to the decrease of both SAC and SAR. Therefore, to further enhance the CDI performance for practical applications, new ion adsorption mechanisms and fine tuning of the pore structure must be considered in a new strategy for the fabrication of CDI electrodes.

In this work, a strategy of using a nanoengineered porous non-carbon electrode for a CDI cell is proposed for the first time. As shown in Fig. 1, the as-prepared 3D ordered mesoporous titanium nitride (3DOM-TiN) functions as the nanoengineered non-carbon electrode for high-performance CDI. Such a novel and rational design adapts the following advantages to maximize CDI performance (Fig. 1): (i) the application of dual ion electrosorption mechanisms, namely EDLC and pseudocapacitance (PC), which significantly enhances the SAC and SAR; (ii) a well-designed ordered hierarchically porous structure together with high surface area and high pore volume, which effectively boosts ion adsorption and decreases ion diffusion resistance, hence maximizing both SAC and SAR; and, (iii) an interconnected nanoframework and nitrogen-doped carbon residual coating, which ensure high electrical conductivity and fast charge transfer, hence further improving CDI performance. As a result, in a batch mode flow-by CDI cell, the 3DOM-TiN electrode delivers a high SAC of 23.6 mg g<sup>-1</sup> and maximum SAR of 3.2 mg g<sup>-1</sup> min<sup>-1</sup> in 500 mg L<sup>-1</sup> NaCl solution at an applied voltage of 1.2 V. Furthermore, it demonstrates

<sup>a</sup>Department of Chemical Engineering, Waterloo Institute for Nanotechnology, University of Waterloo, Waterloo, Ontario N2L3G1, Canada. E-mail: zhwchen@uwaterloo.ca; aipingyu@uwaterloo.ca

<sup>b</sup>Department of Chemical and Biological Engineering, University of Ottawa, Ottawa, Ontario K1N 6N5, Canada. E-mail: Jason.zhang@uottawa.ca

† Electronic supplementary information (ESI) available. See DOI: 10.1039/c9ta04025k

‡ These authors have contributed equally to this work.

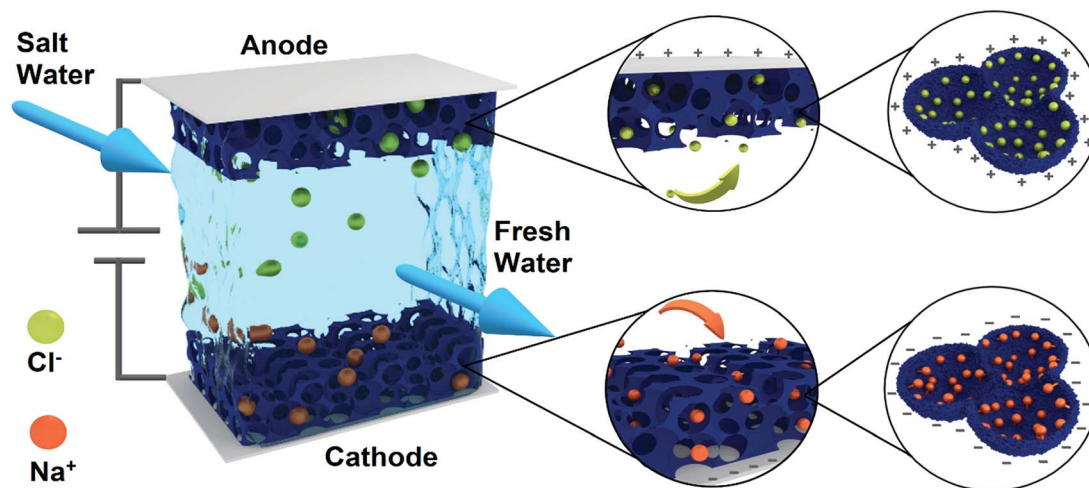


Fig. 1 Schematic of 3D hierarchically ordered mesoporous titanium nitride as the electrode for capacitive deionization.

a superior regeneration and cycling stability to that of the AC electrode. The superior CDI performance of the 3DOM-TiN electrode not only provides promising CDI applications but also highlights the effective strategy of employing nano-engineered non-carbon electrode designs for next-generation CDI devices.

The synthesis of 3DOM-TiN follows the typical templating method depicted in Fig. S1.†<sup>19,20</sup> The Experimental details can be seen in the ESI.† A 3D ordered polystyrene (PS) template was infiltrated with titanium butoxide to form the PS/sol-gel composite. Then, the composite was annealed under an argon atmosphere to remove the PS template followed by a nitridation process with  $\text{NH}_3$  at  $800^\circ\text{C}$  to obtain 3DOM-TiN. For comparison, a bulk-TiN sample was synthesized through a similar sol-gel-annealing-nitridation process without the introduction of the PS template. As demonstrated by scanning electron microscopy (SEM) and transmission electron microscopy (TEM) images in Fig. 2a, b & S2,† the interconnected ordered hierarchically porous 3D nanostructure is obtained through such a synthesis procedure. These images match with the BET analysis results in Fig. 2c, showing the ordered hollow macropores with a size of approximately 100 nm and the connecting mesopores with a size of 12.7 nm. The scattered nanoparticles and the rough pore walls in the magnified TEM images are related to the sol-gel and nitridation process. This process creates small mesopores of less than 10 nm for both 3DOM-TiN and bulk-TiN (Fig. 2c & S3†). The hierarchical macro-/mesoporous structure provides 3DOM-TiN with a high surface area of  $141.6\text{ m}^2\text{ g}^{-1}$ , over four times larger than that of bulk-TiN ( $31.65\text{ m}^2\text{ g}^{-1}$ , Table S1†) and significantly larger than the surface areas of previously reported TiN materials.<sup>21,22</sup> This maximizes the electrolyte-electrode interfaces and improves the electrosorption capacity of  $\text{Na}^+$  and  $\text{Cl}^-$  onto the electrode during the CDI process. Moreover, according to Table S1,† the interconnected macropores also provide 3DOM-TiN with nearly ten times higher pore volume in comparison with that of bulk-TiN ( $0.291\text{ cm}^3\text{ g}^{-1}$  vs.  $0.030\text{ cm}^3\text{ g}^{-1}$ ). This allows the absorption of bulk saline electrolyte into its structure, which will

extend the electrolyte-electrode interface into 3DOM-TiN and minimize the ion diffusion distance from bulk saline water to the electrode surface during the CDI process.

The successful nitridation of both 3DOM-TiN and bulk-TiN is confirmed using the X-ray diffraction (XRD) patterns (Fig. 2d). The major peaks at  $36^\circ$ ,  $42^\circ$ ,  $62^\circ$ ,  $75^\circ$ , and  $80^\circ$  are assigned to TiN crystal planes (111), (200), (220), (311), and (420), respectively. Despite the existence of the two minor rutile  $\text{TiO}_2$  peaks, 3DOM-TiN shows much higher purity in comparison with bulk-TiN. The slight downshift of XRD peaks in 3DOM-TiN as opposed to bulk-TiN further proves the higher degree of nitridation in 3DOM-TiN according to the calculation in Table S2.†<sup>23,24</sup> Such a high purity and degree of nitridation are attributed to the 3D interconnected porous structure which allows high diffusion and thorough reaction with  $\text{NH}_3$  during the nitridation process.

Both the energy-dispersive X-ray spectroscopy (EDX) results in Fig. S4† and the X-ray photoelectron spectroscopy (XPS) survey in Fig. S5a† reveal the existence of O and C on the surface of 3DOM-TiN (Table S3†). In addition, according to the EDX map in Fig. S4c-e,† they are well distributed together with Ti and N. This indicates that surface oxidation and residual carbon coating from the removal of PS templates occur at the surface of 3DOM-TiN.<sup>20</sup> The surface oxidation of 3DOM-TiN occurs when it is exposed to air,<sup>25</sup> generating high oxidation state Ti species such as  $\text{TiO}_x\text{N}_y$  and  $\text{TiO}_2$  on its surfaces according to the high-resolution Ti 2p, N 1s, and O 1s XPS spectra in Fig. 2e, f & S5b.† These Ti species with various oxidation states on the high surface area 3DOM-TiN potentially allow fast surface faradaic reactions through the oxidation/reduction of these Ti species during the electrochemical charge and discharge processes.<sup>26,27</sup> Also, these species can facilitate fast surface intercalation/deintercalation of sodium ions to further enhance ion electrosorption capacity.<sup>28-30</sup> The residual carbon coating from the PS template is found to be doped with nitrogen, mainly forming pyridinic nitrogen in the carbon structure (Fig. 2f & S5c†). Such a nitrogen-doped carbon (NCR) coating can not only enhance the electronic conductivity

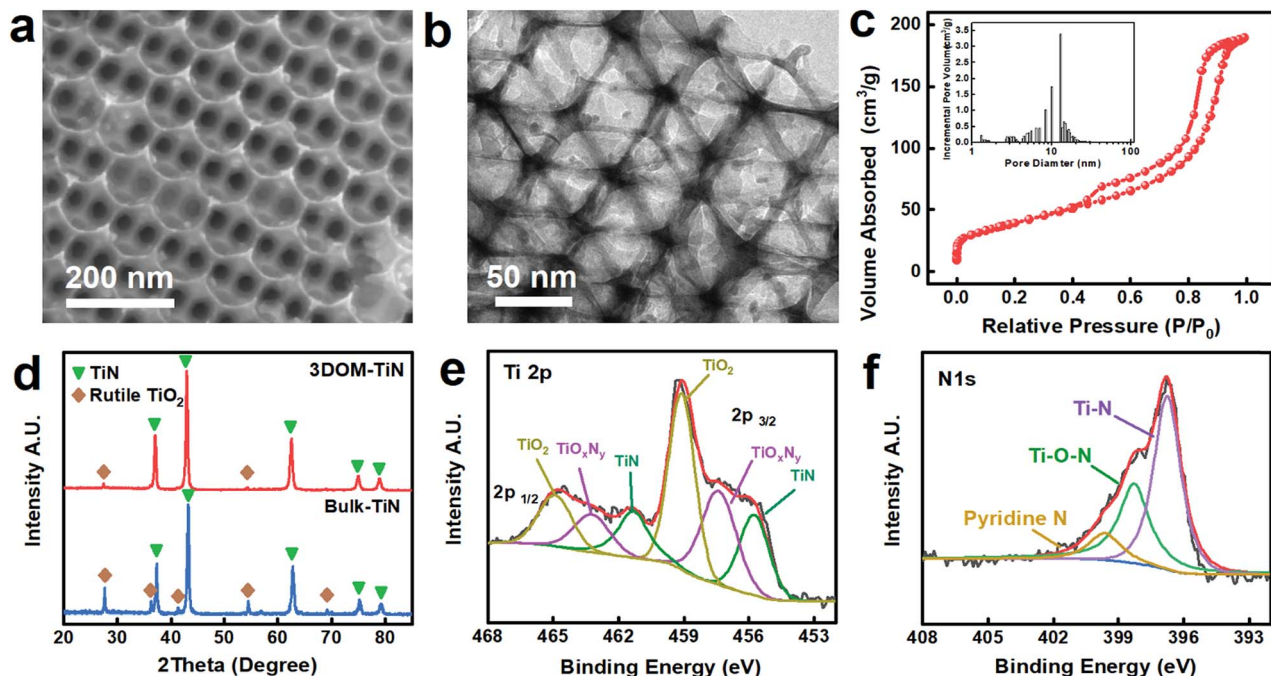


Fig. 2 (a) SEM and (b) TEM images of 3DOM-TiN; (c)  $N_2$  adsorption–desorption isotherm and associated pore size distribution of 3DOM-TiN; (d) XRD patterns of 3DOM-TiN and bulk-TiN; high resolution XPS spectra of (e) Ti 2p and (f) N 1s.

of 3DOM-TiN to indirectly improve CDI performance, but also directly contribute potential extra SAC for 3DOM-TiN during the CDI process.<sup>31,32</sup> Additionally, these polar oxygenated species on the surface of 3DOM-TiN shown in Fig. S5b† can form hydrogen bonds with water and hence enhance the wettability of the electrode and benefit the ion storage process in 3DOM-TiN.<sup>33,34</sup>

The electroadsorption performance of the electrodes was first investigated *via* cyclic voltammetry (CV) in a typical three-electrode system in  $1 \text{ mol L}^{-1}$  NaCl aqueous solution, employing a saturated calomel electrode (SCE) and a graphite rod as the reference electrode and the counter electrode, respectively. The CV curves of 3DOM-TiN, bulk-TiN, and AC electrodes in Fig. 3a are all quasi-rectangular in shape, showing the considerable contribution of EDLC in all three electrodes. The additional distinct redox peaks located at  $-0.23 \text{ V vs. SCE}$  in the CV curves of both 3DOM-TiN and bulk-TiN show the existence of pseudocapacitance. Overall, the specific capacitance of the 3DOM-TiN electrode ( $142.9 \text{ F g}^{-1}$ ) is larger than that of the AC electrode ( $88.9 \text{ F g}^{-1}$ ) and the bulk-TiN electrode ( $45.4 \text{ F g}^{-1}$ ) at a scan rate of  $50 \text{ mV s}^{-1}$  (Fig. 3a). The dramatic enhancement of the specific capacity of the 3DOM-TiN electrode is strongly related to the increase of surface area brought by the 3D hierarchically porous interconnected nanostructure, which increased the efficiency of utilizing the active sites and enhanced the ion diffusion from the electrolyte to the internal porous structure of 3DOM-TiN.<sup>35,36</sup> When varying scan rates are applied to the 3DOM-TiN electrode, the CV curves maintain the quasi-rectangular shape (Fig. 3b), and the obtained specific capacitance can reach as high as  $171.1 \text{ F g}^{-1}$  at  $5 \text{ mV s}^{-1}$  (Fig. 3c). At every scan rate, the 3DOM-TiN electrode outperforms the AC and bulk-TiN electrodes with approximately 50%

and 200% larger specific capacitance, respectively (Fig. 3c & S6†), thus indicating its superior electroadsorption performance during the CDI process. The specific capacitance of 3DOM-TiN also increases with the concentration of NaCl (Fig. S7†) in the low electrolyte concentration range ( $0.1\text{--}1.0 \text{ mol L}^{-1}$ ). Furthermore, the 3DOM-TiN electrode demonstrates excellent stability,

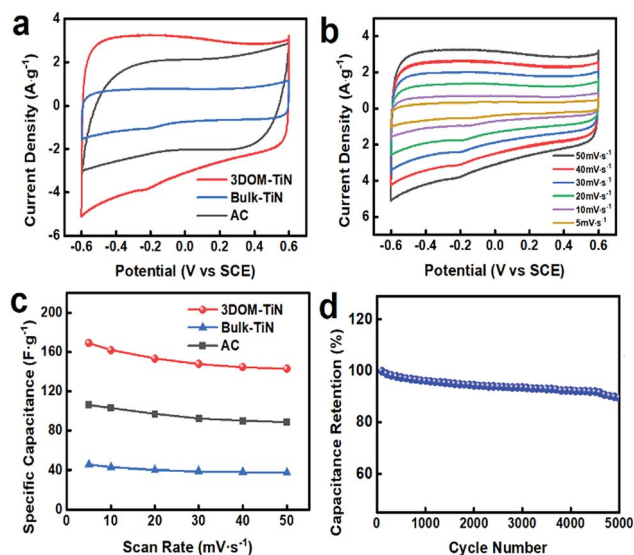


Fig. 3 (a) CV curves of 3DOM-TiN, AC and bulk-TiN electrodes in  $1.0 \text{ mol L}^{-1}$  NaCl solution with a scan rate of  $50 \text{ mV s}^{-1}$ ; (b) CV curves of 3DOM-TiN electrodes in  $1.0 \text{ mol L}^{-1}$  NaCl solution with various scan rates; (c) specific capacitance of 3DOM-TiN, AC and bulk-TiN electrodes in  $1.0 \text{ mol L}^{-1}$  NaCl solution under different scan rates; (d) cycling stability of the 3DOM-TiN electrode up to 5000 cycles.

showing over 90% retention of its initial capacitance after 5000 cycles at a scan rate of  $50 \text{ mV s}^{-1}$  in  $1.0 \text{ mol L}^{-1}$  NaCl solution (Fig. 3d), indicating its excellent stability in the CDI cell. Additionally, the high-resolution C 1s XPS of 3DOM-TiN after cycling shows an insignificant decrease of  $\text{sp}^2$  hybridized carbon ( $\sim 4\%$ ) and slight increase of oxygenated carbon species and  $\text{sp}^3$  hybridized carbon (Fig. S8<sup>†</sup>), indicating sufficient stability and resistivity to oxidation of the NCR-coating for CDI applications.

To further understand the electrochemical properties and electroadsorption behavior of the electrodes, electrochemical impedance spectroscopy (EIS) was conducted for both 3DOM-TiN and bulk-TiN electrodes. The Nyquist plots of both electrodes in Fig. 4a show an incomplete semicircle in the high-frequency region and a steep straight line in the low-frequency region. The associated equivalent circuit model, shown as an inset, in Fig. 4a successfully accounted for the resistive and capacitive features of the electrodes.<sup>37,38</sup> Both the smaller equivalent series resistance ( $R_s$ ) as shown in Fig. S9a<sup>†</sup> ( $4.07 \Omega$ ) and the larger electronic conductivity ( $562.7 \text{ S m}^{-1}$ ) of 3DOM-TiN as shown in Fig. 4b relative to bulk-TiN ( $8.69 \Omega$ ,  $317.5 \text{ S m}^{-1}$ ) suggest an enhanced electronic transfer due to the interconnected 3D nanostructure and NCR-coating within the 3DOM-TiN electrode. This inevitable stable NCR-coating will contribute to the CDI performance indirectly *via* the enhancement of electrical conductivity. According to the literature,<sup>34,37,38</sup> the two constant phase elements (CPEs), namely CPE1 and CPE2, are assigned to EDLC and PC, respectively. The charge transfer resistance ( $R_{ct}$ ) is connected in series with CPE2 and mainly indicates the resistive behavior at the electrode–electrolyte interface occurring during the pseudocapacitive charge

storage process. The observed lower  $R_{ct}$  of the 3DOM-TiN electrode as opposed to that of the bulk-TiN electrode ( $9.62 \Omega$  vs.  $17.61 \Omega$ ) (Fig. S9a<sup>†</sup>) reveals the fast kinetics of the faradaic reactions occurring at the highly exposed accessible active sites on the surface of the interconnected hierarchically porous 3DOM-TiN electrode. It is also observed in Fig. 4a that the linear straight line exhibited by 3DOM-TiN in the low-frequency region is steeper than that of the bulk-TiN electrode, implying faster ion diffusion in the 3DOM-TiN electrode. The calculated Warburg coefficient  $\sigma$  ( $\Omega \text{ s}^{-0.5}$ ) in Fig. S9b<sup>†</sup> demonstrates that the ion diffusion resistance of 3DOM-TiN is only 12% of the value of that in the bulk-TiN electrode. These results prove that the 3D interconnected hierarchically porous nanostructure enables fast ion diffusion from the electrolyte to the electrode, fast pseudocapacitive charge storage and high electronic conductivity, thus endowing the 3DOM-TiN electrode with a high specific capacitance and great potential as a CDI electrode.

Investigations of the electrochemical behavior of 3DOM-TiN as both the anode and cathode were also conducted *via* CV measurement. As illustrated in Fig. 4c, the 3DOM-TiN cathode delivers a slightly higher specific capacity than the 3DOM-TiN anode at a scan rate of  $10 \text{ mV s}^{-1}$  ( $90.2 \text{ F g}^{-1}$  vs.  $66.5 \text{ F g}^{-1}$ ). Such a difference between electroadsorption towards the cation ( $\text{Na}^+$ ) and anion ( $\text{Cl}^-$ ) lies in the difference in sorption mechanisms of each specific ion.<sup>39,40</sup> Nevertheless, Fig. 4c indicates that the 3DOM-TiN electrode has high electroadsorption capacity towards both cations and anions, which is a desirable property for electrodes used in the symmetric design of CDI. To quantify the contribution of capacitive ion sorption mechanisms, Dunn's method is employed for the 3DOM-TiN electrode in the anodic and cathodic ranges as well as the full potential range.<sup>9,37,38</sup> The calculation in Fig. S10<sup>†</sup> and the shaded areas in Fig. 4d reveal that EDLC and PC contribute equally in the 3DOM-TiN cathode while EDLC dominates the electroadsorption in the 3DOM-TiN anode (81.8%). Therefore,  $\text{Cl}^-$  is mainly adsorbed onto the hierarchically porous 3DOM-TiN electrode *via* the formation of EDL, which is in line with the literature.<sup>26</sup> Given the highly oxygen-deficient and reductive atmosphere during the nitridation process, a large amount of oxygen vacancies (OVs) must be generated on the surface of 3DOM-TiN during ammonia heat treatment.<sup>19</sup> These OVs on TiN or hydrogenated  $\text{TiO}_2$  have been reported to be responsible for their excellent pseudocapacitance *via* the oxidation/reduction of surface hydroxyl groups and  $\text{OH}^-$  ion adsorption in the chloride-free aqueous electrolyte.<sup>28,41–43</sup> Therefore, it is assumed that the OVs on the surface of 3DOM-TiN can act as non-selective adsorbing sites towards anions in NaCl solution ( $\text{Cl}^-$ ,  $\text{OH}^-$ , etc.) to contribute to the pseudocapacitance at the anode. On the other hand,  $\text{Na}^+$  tends to be electro-adsorbed onto the 3DOM-TiN electrode *via* the fast surface faradaic reaction in addition to the EDL formation. This faradaic  $\text{Na}^+$  storage mechanism takes place at the interface between partially oxidized  $\text{TiO}_x\text{N}_y$  moieties and the electrolyte *via* the oxidation/reduction of Ti during chemisorption or intercalation/deintercalation which is represented by the following reaction.<sup>26–28</sup>

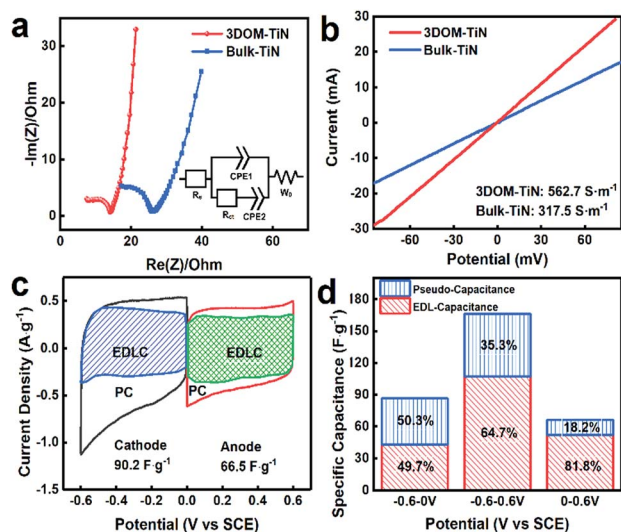
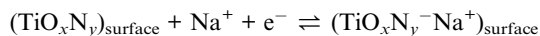


Fig. 4 (a) Nyquist plot and the associated equivalent circuit derived for 3DOM-TiN and bulk-TiN; (b) powder conductivity test of 3DOM-TiN and bulk-TiN; (c) Dunn method analysis of capacitance contribution of the 3DOM-TiN anode and cathode at a scan rate of  $10 \text{ mV s}^{-1}$  in  $1 \text{ mol L}^{-1}$  NaCl solution. The shaded regions show the current contributions from the electrical double-layer capacitive processes; and associate (d) EDLC and PC contribution to specific capacitance of the 3DOM-TiN electrode in the cathodic, anodic and full range.



Therefore, the pseudocapacitive electrosorption of  $\text{Na}^+$  accounts for the majority of PC in the 3DOM-TiN electrode in the full range (Fig. 4d). As a result, the 3DOM-TiN electrode is proved to apply the dual ion electrosorption mechanism to store NaCl simultaneously. Such a mechanism resembles the working principle of a hybrid system of batteries and supercapacitors, such as lithium or sodium ion supercapacitors.<sup>44,45</sup> In this case,  $\text{Na}^+$  ions are stored at the electrode–electrolyte interface at the cathode *via* EDLC and PC, while the counter ions,  $\text{Cl}^-$  ions, are mainly stored in the EDL to balance the charges and transfer extra electrons at the anode. The novel mechanism will enable efficient desalination in the CDI process.

The evaluation of CDI performance was conducted in a flow-by mode symmetrical CDI cell equipped with the 3DOM-TiN, bulk-TiN or AC electrode. Fig. S11<sup>†</sup> shows the comparison of the conductivity profiles of desalinated water against the operation time for the three electrodes in a full batch-mode CDI process at an applied voltage of 1.2 V with  $100 \text{ mg g}^{-1}$  NaCl solution pumped through the cell at a flow rate of  $5 \text{ mL min}^{-1}$ . This shows that all three electrodes took roughly 25 minutes to reduce the solution conductivity to its minimum and then gradually reached a saturated adsorption state around 60 minutes. Correspondingly, the SACs of each electrode at different desalination times were calculated according to Fig. S12<sup>†</sup> and were plotted as a function of time in Fig. 5a. 3DOM-TiN achieves the highest SAC among these three electrodes, specifically  $22.1 \text{ mg g}^{-1}$  at 60 min, which is roughly 4 times and 40% higher than the SAC of bulk-TiN and AC electrodes, respectively. Most importantly, such a high SAC at low salinity ranks the 3DOM-TiN electrode at the top of the best previously reported titanium-based CDI electrodes (Table S4<sup>†</sup>). To compare the desalination efficiency of the CDI electrodes, the SARs of three electrodes were calculated and plotted against SAC in the CDI Ragone plot in Fig. 5b. The SAR increases quickly within the initial 10 min due to the rapid infusion of salt water and then decreases due to the gradual saturation of ion adsorption. Clearly, the 3DOM-TiN electrode shows the highest SAR among these three samples, reaching a maximum SAR of  $0.81 \text{ mg g}^{-1} \text{ min}^{-1}$  which is 2 times and 4 times higher than that of AC and bulk-TiN electrodes, respectively. Such effective and efficient CDI performance of the 3DOM-TiN electrode, showing both high capacity and high rate, is ideal for the CDI process.<sup>46</sup> The dramatic increase of CDI performance with respect to bulk-TiN is strongly related to the nanoengineered features of 3DOM-TiN. First, the high surface area of 3DOM-TiN exposes a large amount of accessible active sites at the electrode–electrolyte interface for dual capacitive deionization mechanisms,<sup>18,39</sup> which greatly increases the SAC. Second, the 3D hierarchically porous structure and high pore volume reduce the ion diffusion resistance, which enhances the SAC and SAR simultaneously. Third, the interconnected nanoframework and nitrogen-doped carbon residual coating ensure high electronic conductivity and efficient charge transfer, which further improves the total

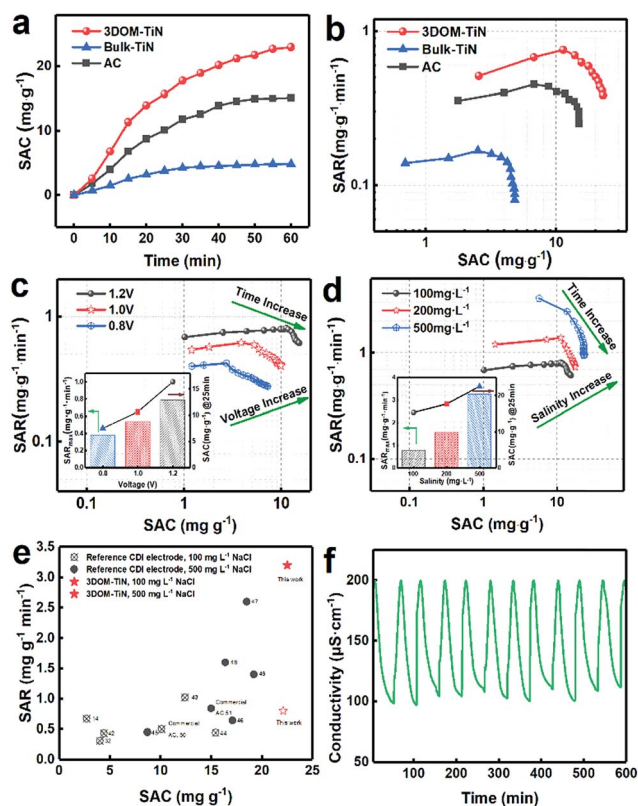


Fig. 5 (a) SAC vs. time and (b) Ragone plot of SAR vs. SAC for 3DOM-TiN, bulk-TiN and AC electrodes obtained from the batch-mode symmetric CDI cell; Ragone plots of SAR vs. SAC for the 3DOM-TiN electrode in a continuous symmetric CDI cell obtained with different operational parameters: (c) cell potential and (d) water salinity; the insert plots illustrate the maximum SAR and SAC at 25 min; (e) SAC and SAR comparison of 3DOM-TiN with recently reported titanium-contained CDI electrodes; (f) Regeneration cycling stability test of the 3DOM-TiN electrode in a continuous symmetric CDI cell with a saline water ( $100 \text{ mg L}^{-1}$  NaCl) flow at  $5 \text{ mL min}^{-1}$  at an applied voltage of 1.2 V.

CDI performance. All these features together make 3DOM-TiN a superior electrode material for CDI.

To further assess the potential of the 3DOM-TiN electrode for practical CDI applications, different operational parameters, namely cell voltage, salinity, and flow rate, were evaluated in the continuous CDI cell, with all desalination processes lasting until the lowest conductivity was reached. The obtained Ragone plots are displayed in Fig. 5c, d & S13.<sup>†</sup> Both SAC and SAR increase together with the applied voltage (Fig. 5c), resulting from the thicker electrical double layer and the stronger coulombic force under the more intense electric field.<sup>47,48</sup> Similarly, the curve in Fig. 5d shifts to the top-right of the CDI Ragone plot as the salinity of the solution increases, indicating the increase of both SAC and SAR at a high salt concentration. When the continuous CDI cell is fed with a solution of  $500 \text{ mg L}^{-1}$  NaCl, the SAC further reached  $23.6 \text{ mg g}^{-1}$  at the saturated adsorption moment, with a maximum SAR of  $3.2 \text{ mg g}^{-1} \text{ min}^{-1}$ . Such a maximum SAR is the highest-ever reported value among all those obtained from carbon and non-carbon-based CDI electrodes (Tables S5 & S6<sup>†</sup>). The 3DOM-TiN

electrode outperforms all recently reported titanium-containing CDI electrodes in terms of the combined performance of SAC and SAR in Fig. 5e.<sup>16,34,49–58</sup> This excellent performance is attributed to two factors; the first being that a higher concentration of ions can enable the formation of a more coherent and denser EDL, and thus more pseudocapacitive ion adsorption and storage at the electrode–electrolyte interfaces.<sup>18</sup> Second, the interconnected hierarchically porous structure and high electronic conductivity of the 3DOM-TiN electrode lower the ion diffusion and charge transfer resistances even at high salinity, hence maximizing the SAR. When the flow rate is adjusted up to 15 mL min<sup>-1</sup>, both the SAC and SAR of the 3DOM-TiN electrode are inferior to those obtained at lower flow rates as shown in Fig. S13.† This decrease could be attributed to the insufficient residence time of the ions in the CDI cell stemming from the high flow rate.<sup>18</sup>

Finally, salt adsorption–desorption cycling tests of the 3DOM-TiN electrode in the CDI cell were conducted to evaluate its stability during the CDI process. The regeneration curve in Fig. 5f demonstrates the continuous and stable performance of over 600 minutes (10 cycles) at an applied potential of 1.2 V and feeding saline water of 100 mg L<sup>-1</sup> NaCl at a flow rate of 5 mL min<sup>-1</sup>. The SAC of the 3DOM-TiN electrode after cycling remains at 15.3 mg g<sup>-1</sup>, representing over 91% retention. It is significantly higher than the retention rate of the AC electrode (73.4%) after 600 minutes cycling (Fig. S14†). Therefore, the 3DOM-TiN electrode exhibited excellent and stable cycling and regeneration abilities. Such high CDI performance of the 3DOM-TiN electrode, especially its high SAC and SAR, demonstrates its promising application as a novel non-carbon CDI electrode for future large-scale desalination treatment of brackish water and seawater.

## Conclusions

In this work, we successfully synthesized 3DOM-TiN using a facile template method and fabricated it into electrodes for batch-mode symmetric CDI cells. The following distinct advantageous features were observed: (i) the high specific capacitance as both the anode and cathode, owing to both the cohesive electrical double layer formed at large accessible electrolyte–electrode interfaces and the fast surface pseudocapacitive reactions involving the bonding of Na<sup>+</sup>; (ii) the well-designed hierarchical 3DOM structure together with high pore volume dramatically decreased the ion diffusion resistances from saline solution to the electrode; and, (iii) the interconnected nano framework and nitrogen-doped carbon residue coating ensured the high electronic conductivity and the low charge transfer resistance. All these features made 3DOM-TiN a promising electrode material in the CDI cell. The 3DOM-TiN electrode delivered an outstanding SAC as high as 23.6 mg g<sup>-1</sup> and a record high maximum SAR of 3.2 mg min<sup>-1</sup> g<sup>-1</sup> in a symmetric CDI cell fed with 500 mg L<sup>-1</sup> NaCl solution. The superior CDI performance not only demonstrates the great potential of the 3DOM-TiN electrode for future CDI applications, but also proposes a feasible and effective strategy of using nanoengineered porous non-carbon electrodes for next-generation CDI cells.

## Conflicts of interest

There are no conflicts to declare.

## Acknowledgements

We acknowledge the Natural Sciences and Engineering Research Council of Canada, the Nanomaterials and Clean Energy Laboratory at the University of Waterloo, the Department of Chemical and Biological Engineering at the University of Ottawa, and the China Scholarship Council.

## Notes and references

- 1 M. Catley-Carlson, *Nature*, 2011, **473**, 27.
- 2 A. Subramani and J. G. Jacangelo, *Water Res.*, 2015, **75**, 164–187.
- 3 J. Choi, P. Dorji, H. K. Shon and S. Hong, *Desalination*, 2019, **449**, 118–130.
- 4 Y. H. Teow and A. W. Mohammad, *Desalination*, 2019, **451**, 2–17.
- 5 M. Andelman, *Sep. Purif. Technol.*, 2011, **80**, 262–269.
- 6 K. Singh, S. Porada, H. de Gier, P. Biesheuvel and L. de Smet, *Desalination*, 2019, **455**, 115–134.
- 7 Y. Zhao, Y. Wang, R. Wang, Y. Wu, S. Xu and J. Wang, *Desalination*, 2013, **324**, 127–133.
- 8 M. Qin, A. Deshmukh, R. Epsztein, S. K. Patel, O. M. Owoseni, W. S. Walker and M. Elimelech, *Desalination*, 2019, **455**, 100–114.
- 9 W. Bao, X. Tang, X. Guo, S. Choi, C. Wang, Y. Gogotsi and G. Wang, *Joule*, 2018, **2**, 778–787.
- 10 V. Chabot, D. Higgins, A. Yu, X. Xiao, Z. Chen and J. Zhang, *Energy Environ. Sci.*, 2014, **7**, 1564–1596.
- 11 L. Lim, Y. Liu, W. Liu, R. Tjandra, L. Rasenthiram, Z. Chen and A. Yu, *ACS Appl. Mater. Interfaces*, 2017, **9**, 39576–39583.
- 12 G. Luo, Y. Wang, L. Gao, D. Zhang and T. Lin, *Electrochim. Acta*, 2018, **260**, 656–663.
- 13 Y. Li, Y. Liu, M. Wang, X. Xu, T. Lu, C. Q. Sun and L. Pan, *Carbon*, 2018, **130**, 377–383.
- 14 Y. Wimalasiri and L. Zou, *Carbon*, 2013, **59**, 464–471.
- 15 T. Gao, F. Zhou, W. Ma and H. Li, *Electrochim. Acta*, 2018, **263**, 85–93.
- 16 H. Yin, S. Zhao, J. Wan, H. Tang, L. Chang, L. He, H. Zhao, Y. Gao and Z. Tang, *Adv. Mater.*, 2013, **25**, 6270–6276.
- 17 H. Wang, L. Shi, T. Yan, J. Zhang, Q. Zhong and D. Zhang, *J. Mater. Chem. A*, 2014, **2**, 4739–4750.
- 18 J. Zhang, J. Fang, J. Han, T. Yan, L. Shi and D. Zhang, *J. Mater. Chem. A*, 2018, **6**, 15245–15252.
- 19 G. Liu, J. Li, J. Fu, G. Jiang, G. Lui, D. Luo, Y. P. Deng, J. Zhang, Z. P. Cano and A. Yu, *Adv. Mater.*, 2018, 1806761.
- 20 G. Lui, G. Li, X. Wang, G. Jiang, E. Lin, M. Fowler, A. Yu and Z. Chen, *Nano Energy*, 2016, **24**, 72–77.
- 21 D. C. Higgins, J.-Y. Choi, J. Wu, A. Lopez and Z. Chen, *J. Mater. Chem.*, 2012, **22**, 3727–3732.
- 22 Z. Xing, G. Li, S. Sy and Z. Chen, *Nano Energy*, 2018, **54**, 1–9.

- 23 I. G. Morozov, O. Belousova, O. Belyakov, I. Parkin, S. Sathasivam and M. Kuznetsov, *J. Alloys Compd.*, 2016, **675**, 266–276.
- 24 R. A. Sait and R. B. M. Cross, *Appl. Surf. Sci.*, 2017, **424**, 290–298.
- 25 B. M. Gray, A. L. Hector, M. Jura, J. R. Owen and J. Whittam, *J. Mater. Chem. A*, 2017, **5**, 4550–4559.
- 26 C. Zhu, P. Yang, D. Chao, X. Wang, X. Zhang, S. Chen, B. K. Tay, H. Huang, H. Zhang and W. Mai, *Adv. Mater.*, 2015, **27**, 4566–4571.
- 27 G. Hasegawa, A. Kitada, S. Kawasaki, K. Kanamori, K. Nakanishi, Y. Kobayashi, H. Kageyama and T. Abe, *J. Electrochem. Soc.*, 2015, **162**, A77–A85.
- 28 X. Lu, G. Wang, T. Zhai, M. Yu, S. Xie, Y. Ling, C. Liang, Y. Tong and Y. Li, *Nano Lett.*, 2012, **12**, 5376–5381.
- 29 J. Dong, Y. Jiang, Q. Li, Q. Wei, W. Yang, S. Tan, X. Xu, Q. An and L. Mai, *J. Mater. Chem. A*, 2017, **5**, 10827–10835.
- 30 Z. Le, F. Liu, P. Nie, X. Li, X. Liu, Z. Bian, G. Chen, H. B. Wu and Y. Lu, *ACS Nano*, 2017, **11**, 2952–2960.
- 31 R. Tjandra, W. Liu, L. Lim and A. Yu, *Carbon*, 2018, **129**, 152–158.
- 32 W. Lei, W. Xiao, J. Li, G. Li, Z. Wu, C. Xuan, D. Luo, Y.-P. Deng, D. Wang and Z. Chen, *ACS Appl. Mater. Interfaces*, 2017, **9**, 28604–28611.
- 33 M. Hashemi, M. S. Rahmanifar, M. F. El-Kady, A. Noori, M. F. Mousavi and R. B. Kaner, *Nano Energy*, 2018, **44**, 489–498.
- 34 A. S. Yasin, H. O. Mohamed, I. M. Mohamed, H. M. Mousa and N. A. Barakat, *Sep. Purif. Technol.*, 2016, **171**, 34–43.
- 35 A. Achour, J. B. Ducros, R. L. Porto, M. Boujtita, E. Gautron, L. Le Brizoual, M. A. Djouadi and T. Brousse, *Nano Energy*, 2014, **7**, 104–113.
- 36 X. Zhou, C. Shang, L. Gu, S. Dong, X. Chen, P. Han, L. Li, J. Yao, Z. Liu, H. Xu, Y. Zhu and G. Cui, *ACS Appl. Mater. Interfaces*, 2011, **3**, 3058–3063.
- 37 Z. Zhou, T. Liu, A. U. Khan and G. Liu, *Sci. Adv.*, 2019, **5**, eaau6852.
- 38 F. Zhang, T. Liu, M. Li, M. Yu, Y. Luo, Y. Tong and Y. Li, *Nano Lett.*, 2017, **17**, 3097–3104.
- 39 C. Costentin, T. R. Porter and J.-M. Savéant, *ACS Appl. Mater. Interfaces*, 2017, **9**, 8649–8658.
- 40 T. Brousse, D. Bélanger and J. W. Long, *J. Electrochem. Soc.*, 2015, **162**, A5185–A5189.
- 41 A. Achour, R. L. Porto, M.-A. Soussou, M. Islam, M. Boujtita, K. A. Aissa, L. Le Brizoual, A. Djouadi and T. Brousse, *J. Power Sources*, 2015, **300**, 525–532.
- 42 A. Achour, J. Ducros, R. L. Porto, M. Boujtita, E. Gautron, L. Le Brizoual, M. Djouadi and T. Brousse, *Nano Energy*, 2014, **7**, 104–113.
- 43 X. Lu, G. Wang, T. Zhai, M. Yu, J. Gan, Y. Tong and Y. Li, *Nano Lett.*, 2012, **12**, 1690–1696.
- 44 J. Ding, Z. Li, K. Cui, S. Boyer, D. Karpuzov and D. Mitlin, *Nano Energy*, 2016, **23**, 129–137.
- 45 Q. Xia, H. Yang, M. Wang, M. Yang, Q. Guo, L. Wan, H. Xia and Y. Yu, *Adv. Energy Mater.*, 2017, **7**, 1701336.
- 46 T. Kim and J. Yoon, *RSC Adv.*, 2015, **5**, 1456–1461.
- 47 G. Trefalt, S. H. Behrens and M. Borkovec, *Langmuir*, 2015, **32**, 380–400.
- 48 M. M. Hatlo, R. Van Roij and L. Lue, *EPL*, 2012, **97**, 28010.
- 49 A. S. Yasin, I. M. Mohamed, H. M. Mousa, C. H. Park and C. S. Kim, *Sci. Rep.*, 2018, **8**, 541.
- 50 A. S. Yasin, M. Obaid, I. Mohamed, A. Yousef and N. Barakat, *ZrO<sub>2</sub> Nanofibers/Activated Carbon Composite as a Novel and Effective Electrode Material for the Enhancement of Capacitive Deionization Performance*, 2017.
- 51 A. G. El-Deen, J.-H. Choi, C. S. Kim, K. A. Khalil, A. A. Almajid and N. A. Barakat, *Desalination*, 2015, **361**, 53–64.
- 52 P. Srimuk, M. Zeiger, N. Jäckel, A. Tolosa, B. Krüner, S. Fleischmann, I. Grobelsek, M. Aslan, B. Shvartsev and M. E. Suss, *Electrochim. Acta*, 2017, **224**, 314–328.
- 53 P.-I. Liu, L.-C. Chung, H. Shao, T.-M. Liang, R.-Y. Horng, C.-C. M. Ma and M.-C. Chang, *Electrochim. Acta*, 2013, **96**, 173–179.
- 54 P. Srimuk, F. Kaasik, B. Krüner, A. Tolosa, S. Fleischmann, N. Jäckel, M. C. Tekeli, M. Aslan, M. E. Suss and V. Presser, *J. Mater. Chem. A*, 2016, **4**, 18265–18271.
- 55 S. Kim, J. Lee, C. Kim and J. Yoon, *Electrochim. Acta*, 2016, **203**, 265–271.
- 56 B. H. Min, J.-H. Choi and K. Y. Jung, *Electrochim. Acta*, 2018, **270**, 543–551.
- 57 R. Zhao, O. Satpradit, H. Rijnaarts, P. Biesheuvel and A. Van der Wal, *Water Res.*, 2013, **47**, 1941–1952.
- 58 K. Dermentzis, *J. Eng. Sci. Technol. Rev.*, 2016, **9**, 130–133.